Research in Astronomy and Astrophysics, 25:055004 (13pp), 2025 May
https://doi.org/10.1088/1674-4527/adc6d9
CSTR: 32081.14.RAA.adc6d9

A New Method to Predict Particle Sizes of Lunar or S-type Asteroid Surfaces Based on The Laboratory Thermal-infrared Data

Yao Xiao[1,2,3], Bin Liu[1,2], Xin Ren[1,2], Da-Wei Liu[1,2], Wan-Qi Zhao[1,2,3], and Juan Xie[1,2,3]
[1] Key Laboratory of Lunar and Deep Space Exploration, Chinese Academy of Sciences, Beijing 100101, China; liub@nao.cas.cn, renx@nao.cas.cn, liudw@nao.cas.cn
[2] National Astronomical Observatories, Chinese Academy of Sciences, Beijing 100101, China
[3] University of Chinese Academy of Sciences, Beijing 100049, China
Received 2025 January 7; revised 2025 March 15; accepted 2025 March 24; published 2025 May 6

Abstract

The surface particle size and distribution characteristics of celestial bodies (e.g., the Moon, asteroids, etc.) will affect the interpretation of hyperspectral remote sensing data and the implementation of sampling missions. Currently, the estimation of the surface particle sizes is mainly focusing on interpreting the thermal inertia with the infrared spectral data from ground-based or space telescopes, but this method show distinct errors compared with the imaging results of the orbiter. By analyzing some thermal infrared spectral data, a relationship between the particle sizes of the main rock-forming minerals (e.g. pyroxene, feldspar, olivine) and the slopes of their thermal infrared spectrum was found. Based on this relationship, a preliminary model for estimating the grain sizes (~30–300 μm) of lunar or S-type asteroids' surfaces which are silicate minerals dominated was established, and the correlation coefficients (R^2) for most of the rock-forming minerals were better than 90%. Six observational datasets of natural lunar and terrestrial samples are used to validate the model, and the results show a systematical overestimation of the ground-truth particle sizes, the potential causes are analyzed and an additional correction is used to eliminate the overestimation of the particle size prediction. These results are expected to provide guidance for interpretation of lunar and S-type asteroid surface sampling and spectral data.

Key words: infrared: planetary systems – minor planets, asteroids: general – techniques: imaging spectroscopy

1. Introduction

The surface particle size and distribution characteristics of the celestial bodies (e.g., the Moon, asteroids, etc.) played an important role in surface landing, roving and sampling. The surfaces of celestial bodies are covered with a thick layer of loose dust, which is unfavorable for landing probes and maneuvering of rovers because of their low load-bearing capacity (Yue et al. 2020). Furthermore, particle size plays a pivotal role in the identification and quantification of material composition through the utilization of Visible and Near-Infrared (VIS-NIR) spectroscopy (Poulet et al. 2007; Ody et al. 2013) and thermal infrared (TIR) spectroscopy (Logan & Hunt 1970; Hunt & Logan 1972; Logan et al. 1973; Mustard & Hays 1997; Shirley & Glotch 2019). For example, the 1 μm absorption position and width of olivine are strongly affected by the particle sizes and become difficult to recognize (Poulet et al. 2007). Previous studies have also shown that particle size has a significant impact on thermal infrared spectral features (e.g., the Christiansen Features (CFs), the Reststrahlen bands (RBs) and the transparency features (TFs), Lyon 1962), causing changes in spectral contrast as well as shifts in positions of CF, RB and TF (Logan & Hunt 1970; Shirley & Glotch 2019). Information regarding particle sizes on the surface of celestial bodies can also facilitate a deeper comprehension of the geological environment, surface-related processes, formation, and evolution of the celestial bodies (Noble et al. 2001; Hamilton et al. 2021).

Currently, a mainstream method of predicting particle size on the surface of celestial bodies is to detect and determine the thermal inertia (Kieffer et al. 1973; Presley & Christensen 1997). Thermal inertia is a measure of how strong the surface materials resist temperature change under the change of solar insolation conditions, and is strongly affected by the regolith particle size and porosity, as well as composition. Therefore, it has been used as an indicator for the particle size for celestial bodies (Emery et al. 2006; Okada et al. 2020; Cambioni et al. 2021). However, due to the uncertainty of thermal inertia modeling which involves a variety of physical parameters (Presley & Christensen 2010; Gundlach & Blum 2013), there are limitations to this approach. According to imaging results aboard the U.S. OSIRIS-REx detector, the surface of the C-type asteroid Bennu is in fact composed mainly of boulders with diameters larger than 1 m (DellaGiustina et al. 2019), which contradicts the notion of a surface dominated by 0.5 ~ 5 cm diameter particles predicted by the thermal inertia derived from the data of the OTES. The particle sizes of Bennu's surface exceed the design specifications of the OSIRIS-REx spacecraft and pose a significant challenge for sampling (Lauretta et al. 2019).

TIR spectroscopy has been playing an important role in particle size prediction and composition identification on the surface of

Table 1
Description of Samples

Sample Type	Specific Mineral Composition	Particle Size Range
Minerals	olivine	(1) 30–54 μm, (2) 54–76 μm, (3) 76–100 μm, (4) 100–150 μm, (5) 150–200 μm, (6) 200–300 μm, (7) 300–450 μm
Mixed sample 1	10wt% augite + 90wt% labradorite	...
Mixed sample 2	30wt% augite + 70wt% labradorite	...
Mixed sample 3	50wt% augite + 50wt% labradorite	...

celestial bodies. Silicate minerals are the main constituents of rocky celestial bodies. The presence of RB, CF and TF in the TIR spectral range is closely related to the composition of silicates, and can be used as an indicator to discriminate their composition. The CF is generally considered to be caused by a rapid change in the refractive index (i.e., anomalous dispersion) of a single molecule prior to its fundamental frequency vibrational band, which is close to that of the refractive index of the medium surrounding it, minimizing backward scattering. Characterized spectroscopically as a reflectance minimum or emissivity maximum, CF can be used as a diagnostic indicator for minerals even when the RB is attenuated (Conel 1969). The RB is caused by the stretching of the Si-O bonds of a silicate mineral and is related to the composition of the mineral itself. The TF exists in the volume scattering region between the Si-O stretching and bending fundamental vibration bands and is characterized as emissivity minima or reflectivity maxima (Salisbury et al. 1991). Shirley & Glotch (2019) detailed the effect of particle sizes on a TIR spectrum under conditions of simulated lunar environments, demonstrating that the spectral contrast of the RBs and TFs is enhanced as particle size decreases, and that the positions of CFs shift to longer wavelengths as particle size decreases (Logan & Hunt 1970; Hunt & Logan 1972; Logan et al. 1973; Mustard & Hays 1997; Shirley & Glotch 2019).

TIR spectrometers have been employed on many space exploration missions. As early as the 1990s, Mariners 6, 7, and 9, all carrying TIR spectrometers (Hanel et al. 1972a, 1972b; Conrath et al. 1973; Pimentel et al. 1974), provided pioneering information on the composition and properties of the Martian surface and atmosphere. The OSIRIS-REx Thermal Emission Spectrometer (OTES) was used to remotely detect mineral and thermophysical properties of the C-type asteroid Bennu (Hamilton et al. 2021). China is about to implement the first asteroid exploration and sample return mission in 2025. As one of the scientific payloads, the Asteroid Thermal Emission Spectrometer (ATES) will perform a TIR spectroscopic survey on the surface of the near-Earth S-type asteroid 2016 HO_3 at different altitudes and different local times (Zhang et al. 2021). Based on the requirements of such a first asteroid sampling and the uncertainty of the particle size prediction, we developed a new method to predict particle sizes based on the TIR spectroscopy. For the same mineral, the slopes of the spectrum near the longer wavenumber side of the CF increases with decreasing particle sizes (Logan & Hunt 1970; Hunt & Logan 1972; Logan et al. 1973; Mustard & Hays 1997; Shirley & Glotch 2019). According to this relationship, we could derive the particle size information by calculating the spectral slopes near the longer wavenumber side of the CF. This method is expected to be useful for future remote sensing and sampling of lunar or S-type asteroids' surfaces, which are silicate mineral dominated.

2. Samples and Data Description

The asteroid 2016 HO3 is thought to be an S-type asteroid with a silicate-dominated composition (Sharkey et al. 2021). Therefore, this study prepared samples of three common silicate minerals (olivine, pyroxene, and feldspar) and their mixtures (Table 1). Each sample was ground into seven distinct particle sizes. Additionally, three groups of mixed samples with varying particle sizes and mass ratios of pyroxene and labradorite were prepared as simplified analogs of gabbro, including (1) mixture of 10wt.% augite and 90wt.% labradorite, (2) mixture of 30wt.% augite and 70wt.% labradorite and (3) mixtures of 50wt.% augite and 50wt.% labradorite. We have known that the average grain size of lunar soils is ~60 μm, and the grain size of lunar soils is also related with depth, with the material at the top of the space weathered layer exhibiting a smaller average grain size (King et al. 1971; King et al. 1972, 1972; McKay et al. 1972, 1974; Carrier 1973; Heiken et al. 1973). Opportunity's exploration of Meridiani Planum on Mars has shown that there is a dark weathering layer near the landing site that is close to 1 m thick and has a grain size of no more than 125 μm (J. Q. Li et al. 2016). Shirley & Glotch (2019) investigated the effect of particle size on TIR spectral features of different minerals in a simulated lunar environment, with seven different particle sizes of <32 μm, 32–63 μm, 63–90 μm, 90–125 μm, 125–250 μm and >250 μm, but there is still a lack of particle size ranges for larger sizes, especially in the range of 250–450 μm. We ground and wet sieved all samples to seven different particle sizes with a wider range of particle sizes (~30–450 μm): 30–54 μm, 54–76 μm, 76–100 μm, 100–150 μm, 150–200 μm, 200–300 μm, and 300–450 μm. Due to the humid summer weather, two mixture samples with particle sizes of 30–54 μm and 54–76 μm experienced agglomeration prior to spectral test. Therefore,

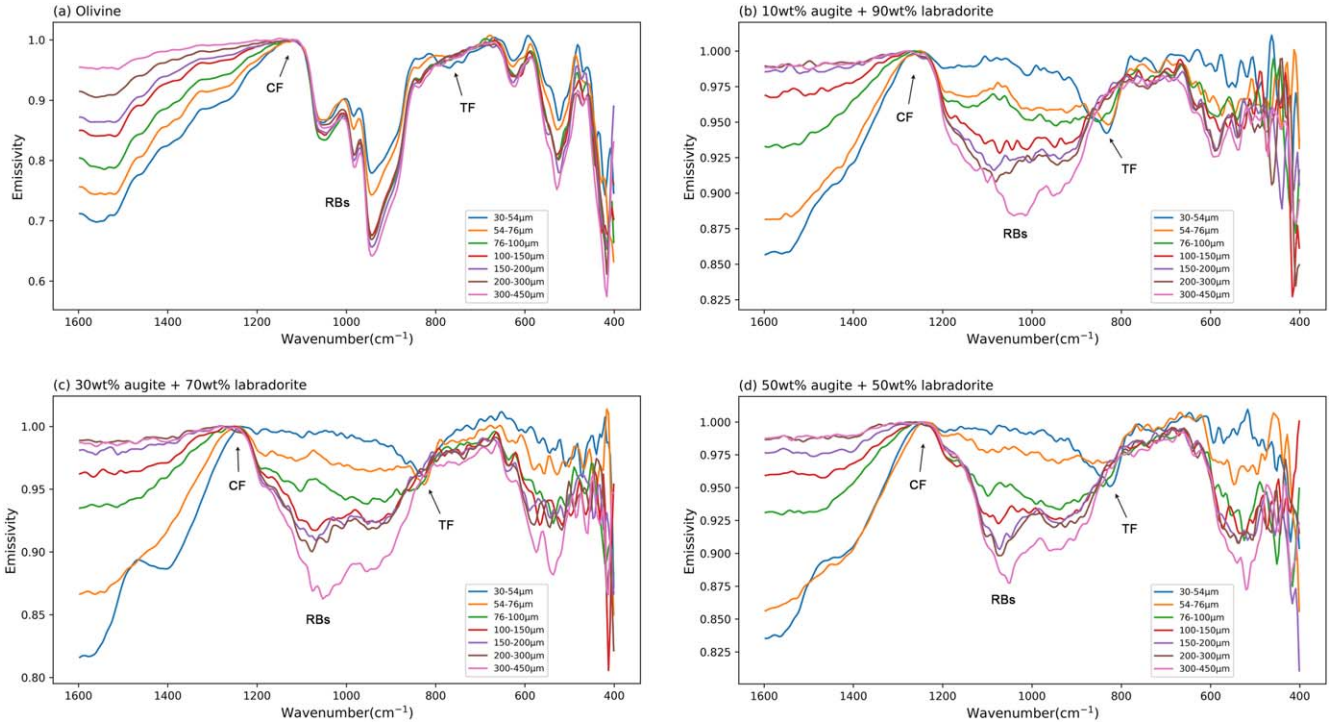

Figure 1. The TIR spectral characteristics of minerals and mixtures with different particle sizes, measured at ordinary atmospheric room temperature. (a) olivine, (b) the mixture with 10wt% augite and 90wt% labradorite, (c) the mixture with 30wt% augite and 70wt% labradorite, and (d) the mixture with 50wt% augite and 50wt% labradorite.

we dried these two mixture samples in an oven with a temperature of 60°C for more than 24 hr before spectral test.

The process of acquiring TIR emissivity spectral data is as follow: The samples were poured into aluminum cups with a diameter of 3 cm to maintain a rough surface similar to that of the natural regolith. The spectral measurements of the samples were carried out using a Bruke 80v Fourier Transform Infrared (FTIR) spectrometer, and reflectance data were first collected using an integrating sphere accessory. The infrared beam enters the integrating sphere and illuminates a deflector mirror mounted inside the sphere, and the deflector mirror directs the infrared beam to the lower sample port and illuminates the samples at an incidence angle of 13°. After that, the reflected and scattered light inside the sphere is collected by the detector located behind the exit port to obtain reflectance data (R). The integrating sphere is a gold-plated integrating sphere with a gold plate as a calibration target. Since the powder samples are thick enough to neglect transmission, the measured reflectance (R) can be converted to emissivity (E) according to the Kirchhoff's law of thermal radiation ($E = 1 - R$). Each sample's spectrum was acquired in the range of 4000–400 cm^{-1} at ambient temperature and pressure, using 128 scans with a resolution of 8 cm^{-1} and a total scanning time of 5 minutes. The spectrum was then normalized by setting the maximum emissivity value to 1. The position of the CF for each sample is obtained by fitting the the maximum emissivity (Donaldson Hanna et al. 2012).

3. Prediction Method for Particle Size

We plotted all the TIR emissivity spectra of the samples with different particle sizes (Figure 1). From Figure 1, a relationship between particle sizes and the slopes of the spectra is found: for the same sample, the spectral slopes close to the longer wavenumber side of the CF gradually become steeper with the decrease of the particle sizes. According to this relationship, we expect to build a new method to predict the particle sizes by calculating the spectral slopes near the longer wavenumber side of the CF. So, it is necessary to ascertain the emissivities and the corresponding wavenumbers at two data points.

One of the data points is undoubtedly the position of the CF and its corresponding emissivity value, According to the TIR spectral characteristics of different minerals, we find that there is usually a rather steep increase in emissivity between the wavenumbers of 2250 cm^{-1}–1333 cm^{-1} and the wavenumbers of 1176 cm^{-1}–870 cm^{-1} as the wavenumbers decrease. The 2250 cm^{-1}–1333 cm^{-1} wavenumber region is dominated by volume scattering, and the 1176 cm^{-1}–870 cm^{-1} region is dominated by surface scattering and the RBs. The sharp increase in emissivity marks the transition from volume scattering to surface scattering, and is therefore referred to by Doug Nash as the "transition edge," which clearly points to the position of the CF feature to be found (Salisbury et al. 1991). To determine the position of the CF feature for each mineral, we defined the CF position by fitting a second-order polynomial to the emissivity

maxima of each mineral spectrum following the method of Donaldson Hanna et al. (2012), and the CF position generally located in the wavenumber range of 1100 cm^{-1}–1400 cm^{-1}. If there was more than one emissivity maximum in the spectrum, we followed the method of Salisbury & Walter (1989) and Cooper et al. (2002) in choosing the emissivity maximum with the longest wavenumbers to fit the CF position.

The other data point should be selected in the wavenumber range of 1700 cm^{-1}–1400 cm^{-1} dominated by volume scattering. Typical particulates of the igneous rocks on a planetary surface often contain hydrated or hydroxylated minerals and will exhibit an H-O-H bending vibration feature near 1613 cm^{-1} (Salisbury & Walter 1989). For olivine and pyroxene, there are also some prominent reflectance absorptions between 2222.2 cm^{-1} and 1333.3 cm^{-1}, which are caused by the absorption of the overtone and combination tone vibrations (Salisbury et al. 1991). In order to circumvent the influence of the aforementioned spectral features, the wavenumber of 1500 cm^{-1} and its corresponding emissivity value are selected as the other data point in the spectral slope calculation. Then the equation to calculate the spectral slope is defined as follows

$$K = \frac{\varepsilon_{CF} - \varepsilon_{1500}}{\omega_{CF} - 1500}. \quad (1)$$

The symbol K represents the spectral slope between 1500 cm^{-1} and the position of CF. The ε_{CF} is the emissivity corresponding to the CF position, ε_{1500} is the emissivity of 1500 cm^{-1} and ω_{CF} is the wavenumber of the CF position.

4. Results and Discussion

4.1. Particle Size Estimation Model

Following the method described in Section 3, we first calculated the CF positions of all the samples (Table 2). The CF positions of olivine vary between 1114 and 1130 cm^{-1} as the grain size changes, with a mean value of ~1122 cm^{-1}. In addition, the CF positions of the mixed sample 1 (90wt% labradorite) fluctuated between 1249 and 1281 cm^{-1}, with a mean value of 1268 cm^{-1}. The CF positions of mixed sample 2 (70wt% labradorite) fluctuate between 1238 and 1281 cm^{-1}, with a mean value of 1258 cm^{-1}, while the CF positions of mixed sample 3 (50wt% labradorite) fluctuate between 1238 and 1249 cm^{-1}, with a mean value of 1249 cm^{-1}. It can be seen that the positions of CF in the mixed samples move toward shorter wavenumbers as the content of labradorite decreases, whereas minerals with a higher magnesium-iron content, such as olivine, have even shorter wavenumbers at the CF position, consistent with all previous observations (Logan & Hunt 1970; Shirley & Glotch 2019).

After the calculation of CF positions for all the samples, we derived the spectral slopes (K-values) following Equation (1). As shown in Table 3, the results of the calculated K-values are consistent with the pattern we observe, and the absolute value of spectral slope increases with decreasing particle size.

Table 2
The CF Positions (cm^{-1}) of Different Samples

Particle Size (μm)	olivine	10wt% augite + 90wt% labradorite	30wt% augite + 70wt% labradorite	50wt% augite + 50wt% labradorite
30–54	1122.50	1253.65	1238.22	1242.08
54–76	1114.78	1249.79	1242.08	1238.22
76–100	1130.21	1265.22	1249.79	1249.79
100–150	1126.36	1272.94	1253.65	1249.79
150–200	1130.21	1276.79	1261.36	1249.79
200–300	1114.78	1276.79	1280.65	1269.08
300–450	1114.78	1280.65	1280.65	1244.65

We further used an exponential function fit to explore the relationship between the K-values and the grain sizes (Figure 2), the result shows that the K-values are first increased when the particle sizes increased, and then the K-values reached their maximum values when the particle sizes increased to ~300 μm, and after that the K-values tended to stabilize with increasing particle sizes. The exponential function is fundamentally modeled as $y = a^*\exp(b^*x) + c$, where the fitting coefficients a, b, c and the correlation coefficient (R^2) are listed in Table 4. The result demonstrates that the exponential function fits were greater than 90% for all samples. Olivine had the best fit. It should be noted that each particle size of the sample has a range, and the mean value of the grain size is employed when plotting the relationship between the K-values and the particle sizes. For example, for the particle size range of 54–76 μm, 65 μm is taken as the horizontal coordinate value.

As illustrated in Figure 1, the spectral curves of the longer wavenumber side for the particle sizes of 200–300 μm and 300–450 μm are overlapped, which makes the K-values of the two particle sizes indistinguishable. There is even a situation in which the K-values of the larger particle sizes are smaller than those of the smaller particle sizes, which is contrary to the pattern previously observed. For example, the K-value for mixture 1 with a particle size of 300–450 μm is less than that of the 200–300 μm case. So, we speculate that the new method we propose to predict the particle sizes may not be applicable for the grain sizes exceeding 300 μm.

From Figure 2, the fitted curves and their corresponding coefficients for the three distinct mixture groups demonstrate striking similarity. With increasing mafic component content (e.g., pyroxene), the curves become progressively flattened (reduced curvature). Notably, the curve for olivine is even more flattened. This indicates that enhanced mafic components correlate with a gradual flattening of the fitted curves, consistent with the observed shift of CF positions toward longer wavelengths at higher mafic concentrations.

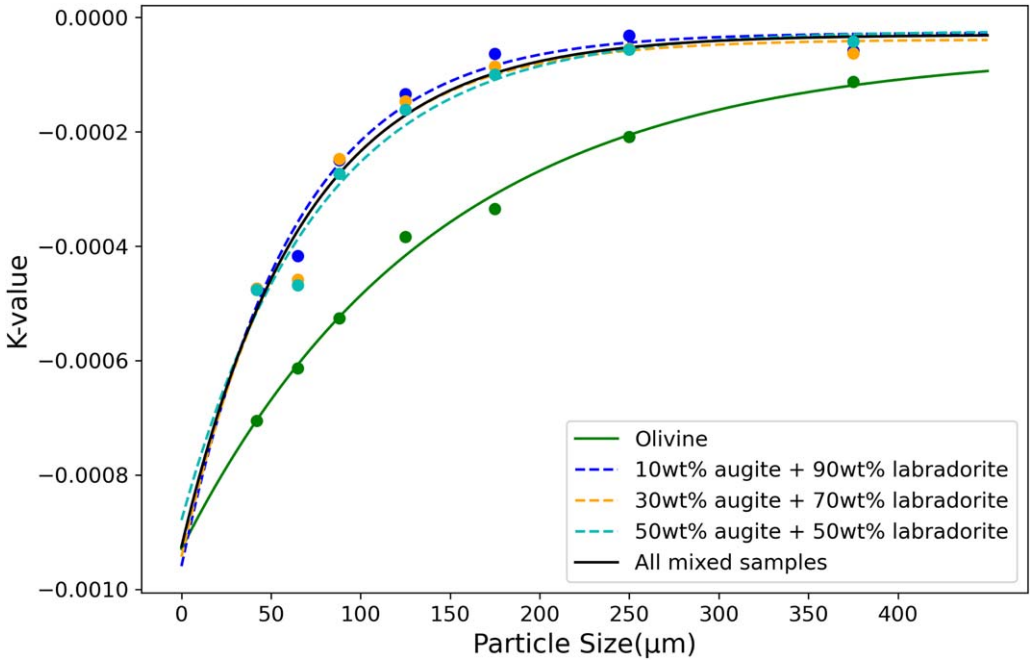

Figure 2. Exponential function fit of the relationship between the particle sizes and the *K*-value.

Table 3
Derived Spectral Slopes (*K*-values) of the Samples With Different Grain Sizes

Particle Size (μm)	olivine	10wt% augite + 90wt% labradorite	30wt% augite + 70wt% labradorite	50wt% augite + 50wt% labradorite
30–54	-7.05×10^{-4}	-4.74×10^{-4}	-4.74×10^{-4}	-4.76×10^{-4}
54–76	-6.14×10^{-4}	-4.17×10^{-4}	-4.59×10^{-4}	-4.68×10^{-4}
76–100	-5.26×10^{-4}	-2.49×10^{-4}	-2.47×10^{-4}	-2.73×10^{-4}
100–150	-3.83×10^{-4}	-1.34×10^{-4}	-1.47×10^{-4}	-1.61×10^{-4}
150–200	-3.35×10^{-4}	-6.34×10^{-5}	-8.55×10^{-5}	-9.97×10^{-5}
200–300	-2.09×10^{-4}	-3.17×10^{-5}	-5.47×10^{-5}	-5.59×10^{-5}
300–450	-1.13×10^{-4}	-5.85×10^{-5}	-6.24×10^{-5}	-4.21×10^{-5}

Table 4
The Coefficients of the Exponential Function Fitting For Each Sample

Sample	***a***	***b***	***c***	R^2
olivine	-8.71×10^{-4}	-7.11×10^{-3}	-5.82×10^{-5}	0.99
10wt% augite + 90wt% labradorite	-9.33×10^{-4}	-1.59×10^{-2}	-2.66×10^{-5}	0.97
30wt% augite + 70wt% labradorite	-9.05×10^{-4}	-1.53×10^{-2}	-3.84×10^{-5}	0.94
50wt% augite + 50wt% labradorite	-8.56×10^{-4}	-1.32×10^{-2}	-2.34×10^{-5}	0.95
All mixed samples	-8.95×10^{-4}	-1.48×10^{-2}	-3.02×10^{-5}	0.95

4.2. Effects of Moisture

The mixture samples in both the 30–45 μm and 45–76 μm particle size classes experienced agglomeration due to the wet weather, and the mixture samples in the 30–45 μm size class are more seriously agglomerated, so the particle sizes are even larger than those of the 45–76 μm size class. To ensure the accuracy of the particle size measurement and to avoid the effect of moisture, we dried the two mixture samples with a drying temperature of 60°C, and the drying time was greater than 24 hr. Oscillation of samples was also carried out after drying to further disperse the agglomerates.

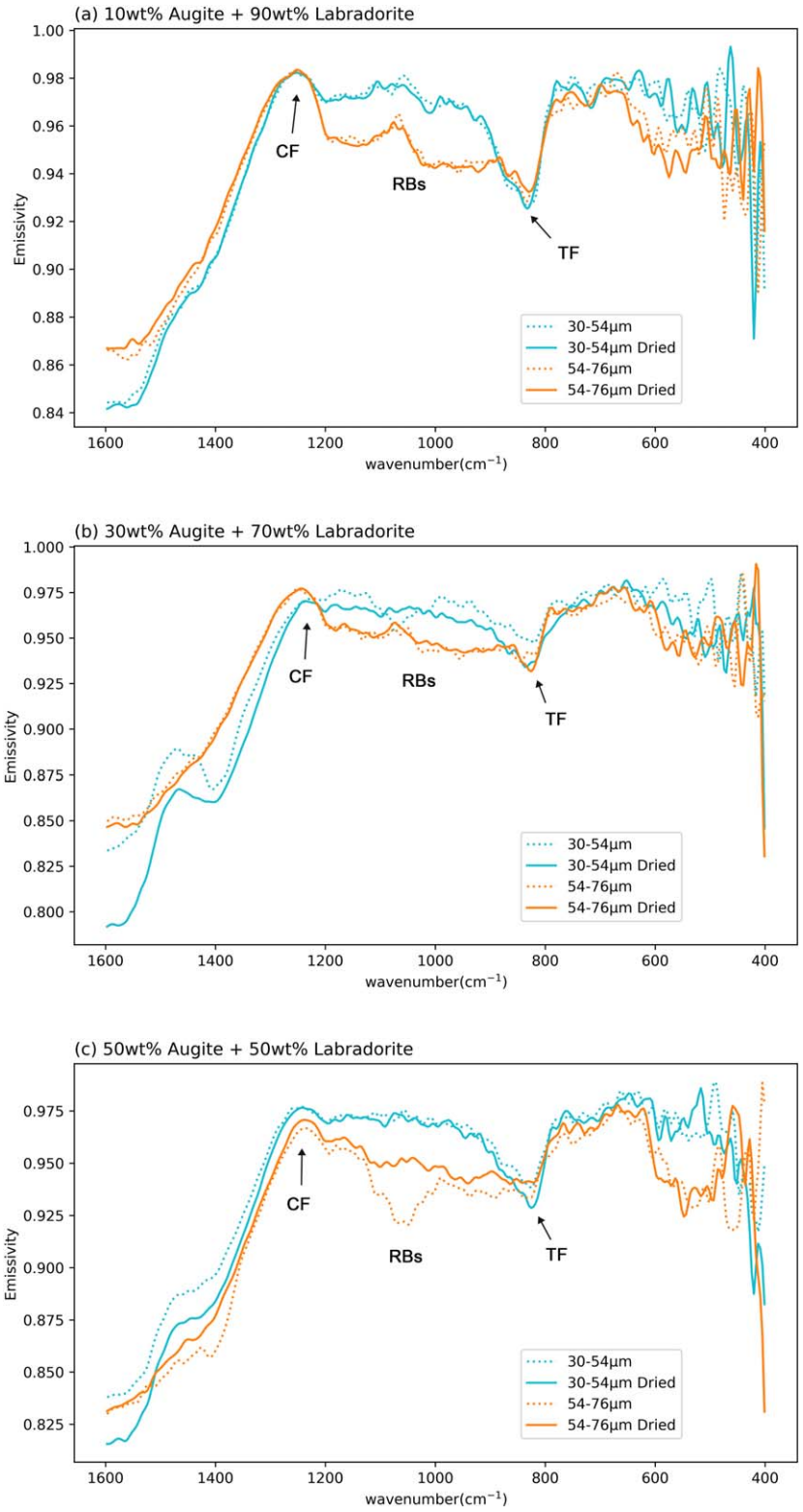

Figure 3. The TIR spectra of the three groups of mixture samples before and after drying in the particle size range of 30–45 μm and 45–76 μm. (a) Mixture sample 1:10wt% augite + 90wt% labradorite; (b) Mixture sample 2:30wt% augite + 70wt% labradorite; and (c) Mixture sample 3:50wt% augite + 50wt% labradorite. (The solid line represents the spectrum after drying, and the dotted line represents the spectrum before drying.)

Table 5
Characteristics of Test Samples

Name	ID	Particle Size (μm)	Specimen Description
Lunar Olivine	LR-CMP-212	0–45	Apollo 15 returned lunar regolith sample: Silicate (Neso), Olivine, Mineral separate from Apollo 15 basalt (LRMCC)
	LR-CMP-169	0–125	...
	LR-CMP-162	125–250	...
Mare Basalt	DD-MDD-036	∼50	Apollo 12 returned lunar regolith sample
	LR-CMP-152	0–125	Apollo 15 returned lunar regolith sample: Basalt, Low-Ti Mare Basalt, Bulk rock separate (LRMCC)
	LR-CMP-153	125–250	...
Gabbro	AN-G1M-011-A	0–63	Natural terrestrial rock sample
	AN-G1M-011-B	63–250	...
	AN-G1M-011-C	250–500	...
	AN-G1M-011-D	500–2000	...
Anorthositic Gabbro	AN-G1M-002-A	0–36	Natural terrestrial rock sample
	AN-G1M-002-B	36–80	...
	AN-G1M-002-C	80–160	...
Apollo lunar regolith	Apollo 15101319	0–25	Apollo 15 returned lunar regolith sample: High-Mg soil sample
		25–63	...
		63–125	...
		125–250	...
	Apollo 6122041	0–25	Apollo 16 returned lunar regolith sample: Immature soil (trench)
		25–63	...
		63–125	...
		125–250	...

Table 6
Modal Mineralogy Estimates of Apollo Lunar Regolith (Data Source: Morlok et al. 2022)

Sample Number	15101319	6122041
MERTIS IRIS database ID	256	257
Sample type	High-Mg soil sample	Immature soil (trench)
Maturity (Is/FeO)	70 (mature)	9.2 (immature)
Bulk Chemistry	...	...
SiO_2	46.29	45.35
TiO_2	1.31	0.49
Al_2O_3	17.7	28.25
Cr_2O_3	0.22	⋯
FeO	11.53	4.55
MnO	0.16	0.06
MgO	10.55	5.02
CaO	11.54	16.21
Na_2O	0.41	0.42
K_2O	0.19	0.09
P_2O_5	0.16	0.1
S	⋯	0.06
SUM	100.06	100.6
Petrogr.	⋯	⋯
Agglut. %	42	6.3
Breccia	7%	33.90%
Fused Soil Comp.	⋯	6.30%
Mineral Frag.	16% Mafic	25.3% Feldspar
	17% Feldspar	...
Glass	17%	19.80%

TIR spectral measurements were conducted on the two classes of mixture samples before and after the drying process (Figure 3). As illustrated in Figure 3, the TIR spectra of the three groups of mixture samples within the 54–76 μm particle size exhibit minimal variation before and after drying, indicating that no moist agglomeration has occurred. In contrast, the emissivity of the three groups of mixture samples in the 30–45 μm particle size on the longer wavenumber side of the CF decreased significantly after drying, and the spectral slope became steeper. This suggests that moisture agglomeration is mitigated to a high extent after drying.

4.3. Physical Mechanism Discussion

We have known the relationship between the thermal spectral slope and the particle size, as the particle size decreases, the absolute value of spectral slope at the longer wavenumber side of the CF feature will increase. The reason for this phenomenon may be as follows: volume scattering dominates for all particle sizes in the wavenumber region close to the CF feature, as the particle size gradually decreases and the sample particles change from optically thick to thin, and the degree of volume scattering gradually increases, leading to lower emissivity or higher reflectivity, and ultimately leading to greater spectral contrast on the longer wavenumber side of the CF (Cooper et al. 2002). Whereas in the weak absorption

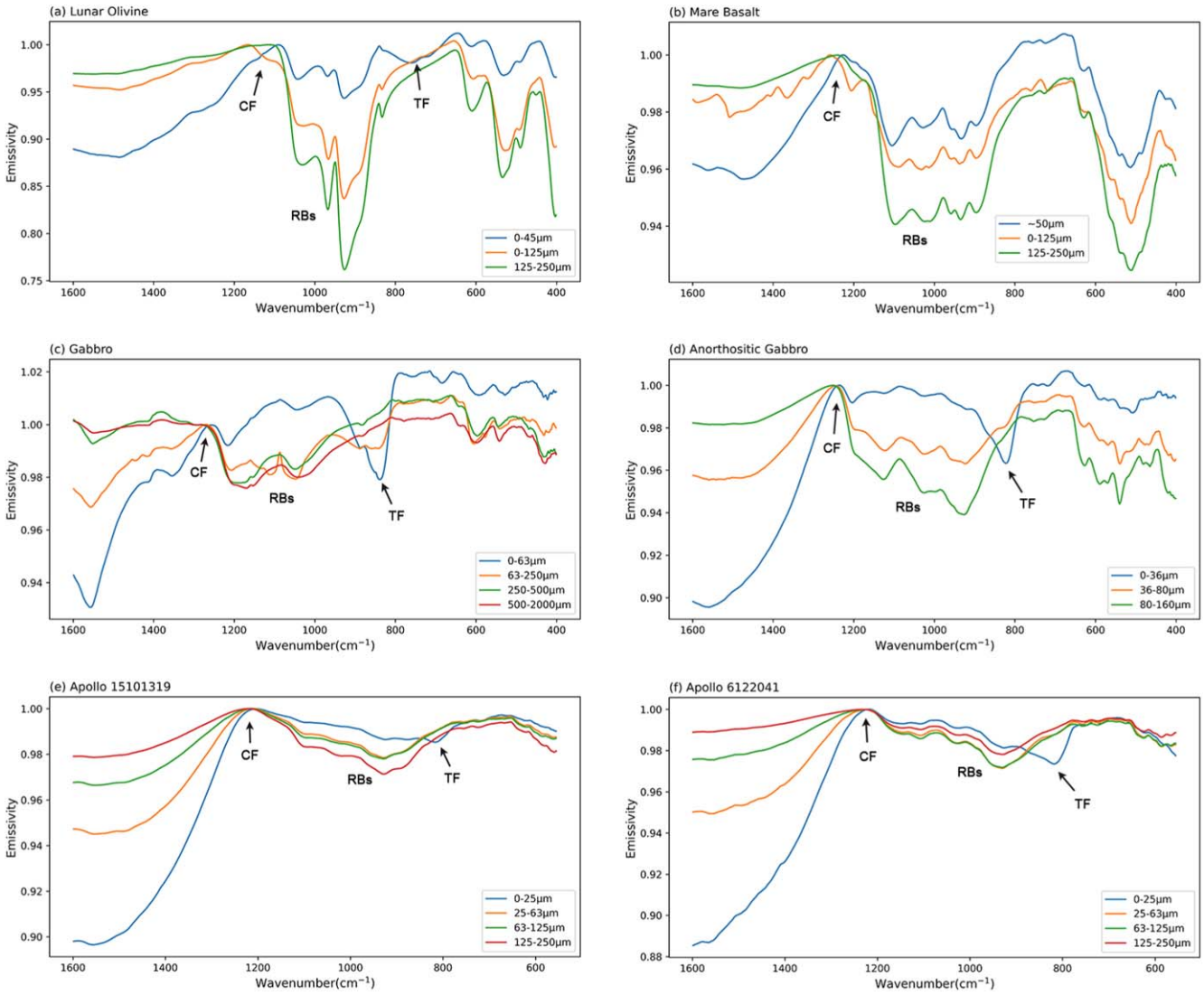

Figure 4. Mid-Infrared Spectra of Test Samples ((a) Lunar Olivine; (b) Mare Basalt; (c) Gabbro; (d) Anorthositic Gabbro; (e) Apollo 15101319; (f) Apollo 6122041).

region of the TIR range, the spectral contrast increases with decreasing particle size due to increased volume scattering (Bishop et al. 2019). Therefore, as the particle size becomes larger, the spectral contrast decreases and the spectral slope K-values converge slowly to zero, a trend that also aligns with the intrinsic convergence behavior of exponential functions. This result also explains why the K-values of the mixture samples with 200–300 μm and 300–450 μm particle sizes are not well differentiated.

4.4. Model Validation and Limitation Discussion

The TIR spectra of four typical samples from the RELAB spectral library are selected for the validation of our particle size prediction model. Typical samples included lunar olivine, lunar mare basalt, and two terrestrial gabbros. To better approximate test data from celestial regolith surfaces, two Apollo lunar soil spectral datasets were additionally selected (data source: Morlok et al. 2022). The particle size characteristics and sample descriptions are detailed in Table 5. Apollo lunar soil spectral data include modal mineralogy results (Table 6). Following Kirchhoff's law ($E = 1\text{-}R$), reflectance data were converted to emissivity spectra (Figure 4). These emissivity data underwent normalization using the methodology in Section 2, with subsequent CF position calculations (Table 7). Figure 4 reveals a consistent trend across lunar and terrestrial samples: finer particle sizes correlate with increasingly steep spectral slopes on the CF's long-wavenumber side.

We calculated spectral slope K for all test samples (Table 7), then the particle sizes of the test samples were subsequently predicted through our model, with results visualized in

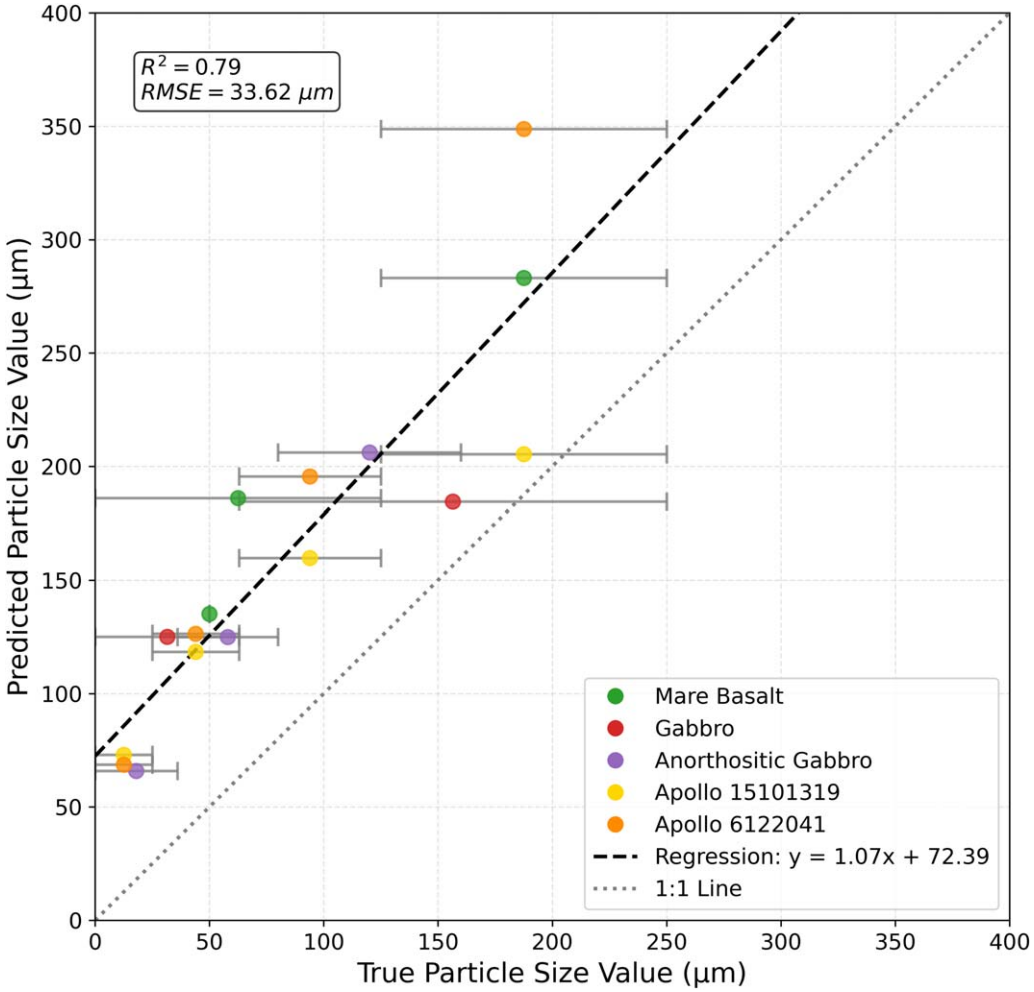

Figure 5. Comparison between predicted and ground-truth particle sizes across test samples. A linear regression method is used to fit the correction formula, see the black dashed line in the figure. The correlation coefficients (R^2) is 0.79, and the RMSE of the fitting is 33.62 μm.

Figure 5. Notably, predictions for specimens AN-G1M-011-C (200–500 μm) and AN-G1M-011-D (500–2000 μm) were excluded from Figure 5 due to exceeding the model's applicable particle size range, as evidenced by their anomalously elevated predictions.

Figure 5 demonstrates that the predicted particle sizes of two Apollo lunar soil groups better match measured values compared to other samples, though most predictions remain systematically higher. This discrepancy may stem from two factors.

First, the analog samples used in our modeling are common silicate minerals, which are ground to single-mineral grains or a mixture of single-mineral grains. However, actual lunar or S-type asteroids' regolith compositions are more complex. Studies on Chang'e-5 returned samples indicate that the lunar regolith typically consists of multi-mineral aggregates, like basaltic fragments, breccia components, glass, and agglutinates (Cao et al. 2025). The freshly ground samples used in our model are single-mineral grains or a mixture of single-mineral grains, which possess brighter surfaces, whereas the natural terrestrial and lunar samples used in model validation are multi-mineral aggregates, which experience weathering effects that darken surfaces and reduce reflectance (Nimura et al. 2008; Wang et al. 2017; Shirley 2018). This weathering particularly diminishes spectral contrast between near-infrared and mid-infrared regions (Yang et al. 2022), leading to higher emissivity values in our study. Consequently, emissivity at 1500 cm^{-1} (ε_{1500}) exceeds modeled values, increasing the K-value. This is likely the primary reason affecting the model's accuracy.

Second, CF position variations contribute to the discrepancy. Comparative spectral analyses between model and test samples (e.g., lunar versus terrestrial olivine in Figure 6, augite-labradorite mixtures versus rock spectra in Figure 7) show that test samples exhibit CF positions either matching or shifted toward lower wavenumbers, which lead to a slight increase in

Table 7
The CF Positions (cm^{-1}) of Test Samples

Name	Particle Size (μm)	CF Position (cm^{-1})	Spectral Slope (K-value)
Lunar Olivine	0–45	1089.61	-2.89×10^{-4}
	0–125	1166.75	-1.41×10^{-4}
	125–250	1114.68	-7.97×10^{-5}
Mare Basalt	~50	1226.53	-1.51×10^{-4}
	0–125	1259.31	-8.73×10^{-5}
	125–250	1240.03	-4.38×10^{-5}
Gabbro	0–63	1257.38	-1.71×10^{-4}
	63–250	1268.95	-8.86×10^{-5}
	250–500	1282.46	-1.36×10^{-5}
	500–2000	1282.46	-8.74×10^{-6}
Anorthositic Gabbro	0–36	1236.17	-3.68×10^{-4}
	36–80	1245.82	-1.71×10^{-4}
	80–160	1251.60	-7.26×10^{-5}
Apollo 15101319	0–25	1203.68	-3.34×10^{-4}
	25–63	1210.11	-1.85×10^{-4}
	63–125	1216.55	-1.14×10^{-4}
	125–250	1220.84	-7.31×10^{-5}
Apollo 6122041	0–25	1218.70	-3.54×10^{-4}
	25–63	1222.99	-1.68×10^{-4}
	63–125	1225.13	-7.98×10^{-5}
	125–250	1229.42	-3.53×10^{-5}

the K-value. CF positions intrinsically depend on mineral composition, with natural samples displaying greater complexity due to heterogeneous mineral proportions (Cooper et al. 2002; Salisbury et al. 1991). Even within mineral groups, CF positions shift with chemical composition. Lunar olivines in Figure 6 exhibit CF positions shifted toward longer wavelengths compared to terrestrial counterparts, attributable to their higher Fe/(Fe+Mg) ratios. Laboratory studies show higher forsterite content shifts CF positions to higher wavenumbers (Hamilton 2010; Lane et al. 2011), consistent with lunar olivines' iron-enriched, magnesium-depleted composition (Yang et al. 2022). Based on the CF position ranges of pyroxene and feldspar (two main constitutes of lunar and S-type asteroids), we estimated that the CF positions of lunar and S-type asteroids could only be located in the wavenumbers of 1180–1288 cm^{-1}, and the particle size prediction errors induced by the CF position variations could be less than 20%.

The combined effects of weathering and CF position shifts synergistically elevate the K-values, ultimately resulting in a systematic overestimation of particle sizes. To enhance the reliability and practical application of our model, we fitted the particle size values between the prediction and the ground truth, and derived a correction formula to eliminate this systematic bias (Figure 5). The formula is $y = \frac{x - 72.39}{1.07}$, where x denotes the predicted values calculated by the particle size estimation model, and y represents the corrected values. The calibrated model demonstrates optimal predictive performance for silicate-dominated regolith surfaces with particle sizes ranging 30–300 μm.

Most extraterrestrial rock fragments may also contain other minerals such as sulfides, phosphates, or glass phases. Glass phases may constitute a significant proportion of lunar regolith and cause "broad and smooth" morphologies in the RB features of reflectance spectra, but they likely do not affect diagnostic CF positions (Nash & Salisbury 1990, see Figure 2 in Morlok et al. 2022). Similarly, some phosphate minerals exhibit distinct spectral features in the ~1200–900 cm^{-1} range due to P-O stretching vibrations (Lane et al. 2011b), but their low abundance in lunar regolith means spectral characteristics remain dominated by silicate minerals (see Figure 2 in Morlok et al. 2022). Sulfides only show significant spectral features below ~450 cm^{-1} (Bishop et al. 2019), thus their influence on the particle size estimation model is negligible.

Although our intimate mixtures of binary mineral particles (augite-labradorite) cannot fully replicate the spectral characteristics of actual regolith surfaces with complex mineralogical

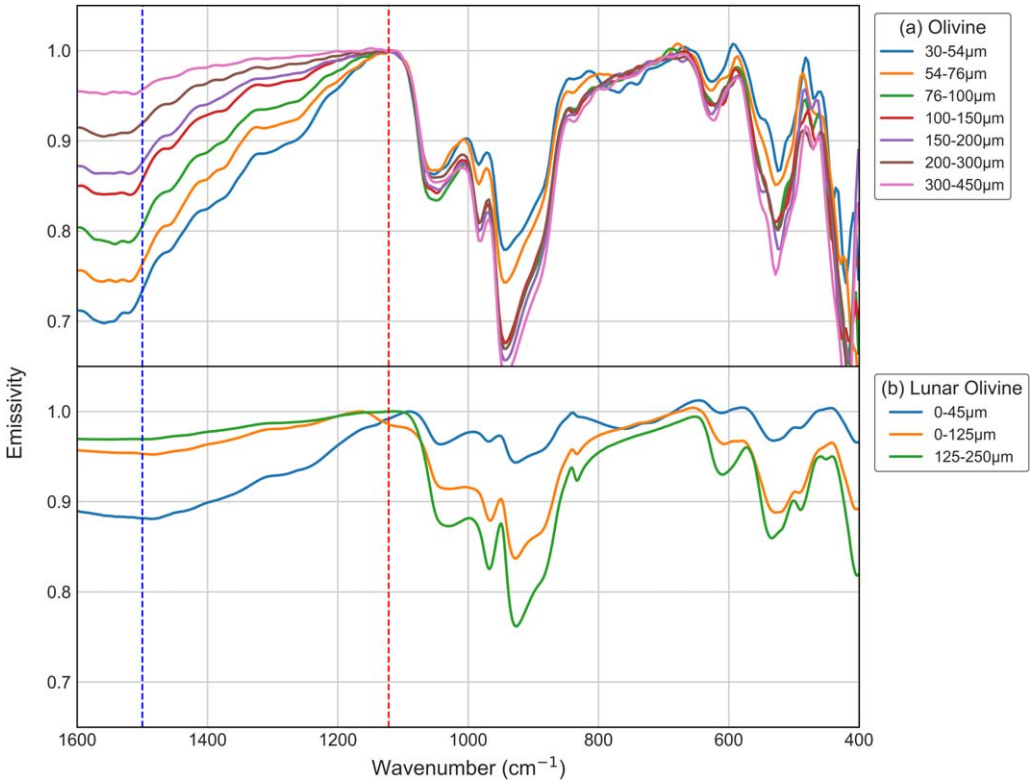

Figure 6. Comparison of CF positions between terrestrial olivine and lunar olivine samples. Red dashed lines mean CF positions of (a) olivine; blue dashed lines indicate the 1500 cm^{-1} reference position.

scenarios, these synthetic mixtures allow controlled isolation of specific physical properties–particularly the relative proportions of mafic versus felsic components–to systematically evaluate their impacts on CF positions. This approach facilitates quantitative assessment of individual factors driving spectral variations. Furthermore, spectra from simple binary mixtures of augite and labradorite provide meaningful analogs for immature lunar regolith particles (Crown & Pieters 1987).

Our particle size estimation model currently demonstrates optimal applicability under two specific scenarios: (1) silicate-dominated surfaces with substantial pyroxene-feldspar assemblages (higher pyroxene-feldspar abundances correlate with enhanced model performance), and (2) regolith-covered terrains where particle sizes fall below $\sim$300 μm. The model is inapplicable to bare bedrock boulders.

5. Summary and Future Work

The results of laboratory studies have demonstrated that the size of mineral particles has a significant effect on the TIR spectra, which in turn affects the ability to identify and interpret the celestial bodies' surface composition. Particle size is also an important factor to be considered in missions such as landing site selection and sampling. However, methods for predicting the particle sizes on the surface of a target object are currently scarce and imperfect. In this study, an analysis of the TIR spectral data of terrestrial minerals and mixtures revealed a correlation between the particle sizes and the slopes of their TIR spectra. Based on this relationship, a new model for predicting the particle sizes of mineral and mixtures is established, which provides a novel idea for predicting the particle sizes on the surface of celestial bodies.

In this study, the new method predicts the particle sizes by analyzing the particle size's influence on TIR spectra. However, the TIR spectral characteristics are also affected by many other factors, especially the presence or absence of atmosphere. Previous experiments have demonstrated that the spectral contrast of the RBs and the TFs are enhanced and the position of the CF feature will be shifted to longer wavelengths as the particle size decreases on the surface of airless objects (Logan & Hunt 1970; Shirley & Glotch 2019). Other influence factors exist such as porosity (Logan et al. 1973; Salisbury & Eastes 1985), surface roughness (Bandfield 2009; Bandfield et al. 2015; Davidsson et al. 2015) and space weathering (Hapke et al. 1975; Glotch et al. 2015; Lucey et al. 2017). These factors are currently not considered in our particle size prediction model, which needs to be further improved in a future investigation. Anyway, our study

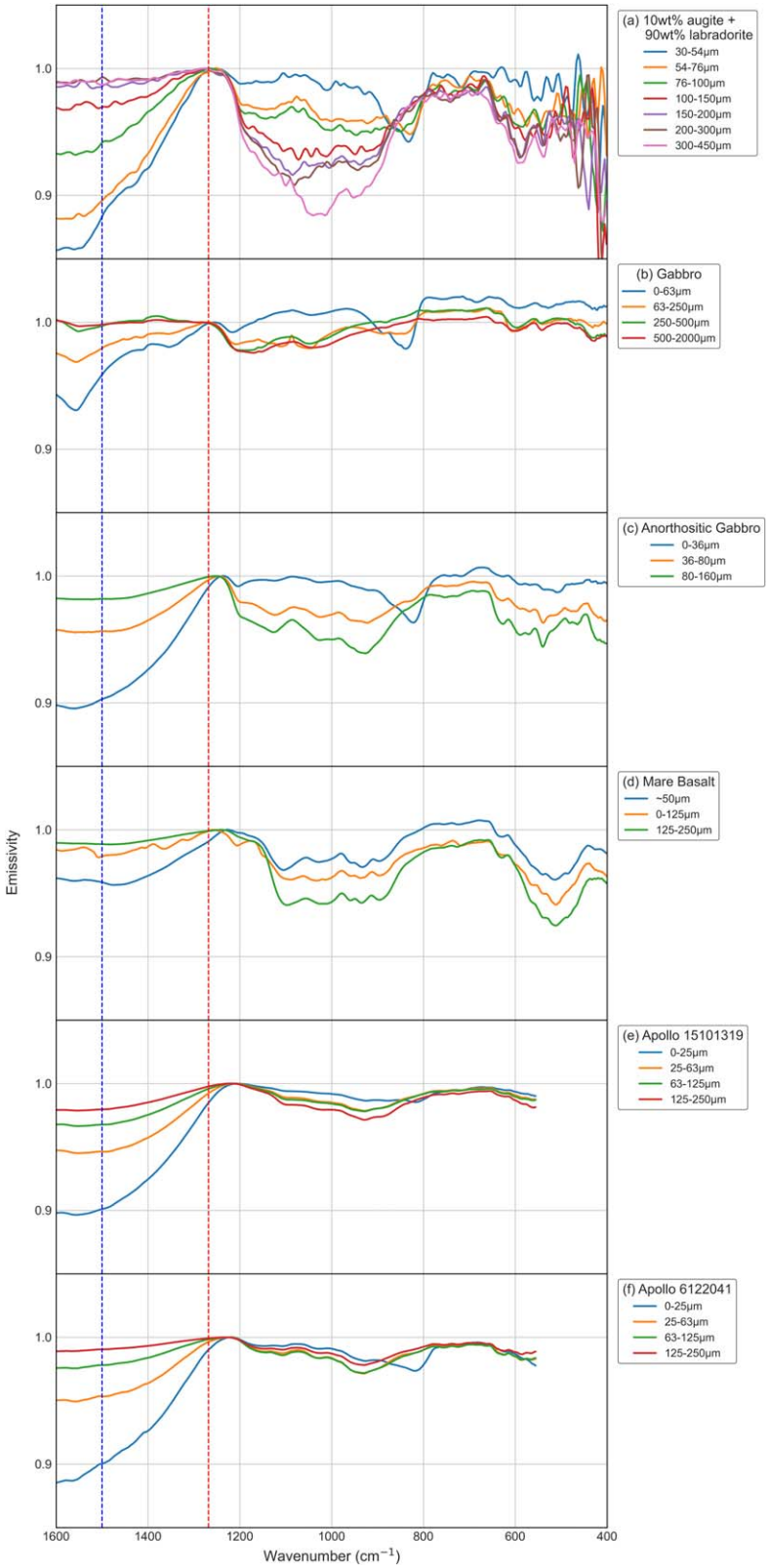

Figure 7. Comparison of CF positions and spectral contrast between modeling analog samples and the validation samples. Red dashed lines mean CF positions of (a) 10wt% augite + 90wt% labradorite; blue dashed lines indicate the 1500 cm^{-1} reference position.

provided a new idea and useful attempt to predict particle sizes on silicate-dominated celestial surfaces.

Acknowledgments

This work was supported by China's first Asteroid exploration program and China National Space Administration (CNSA), and was also funded by the National Natural Science Foundation of China (NSFC, Grant No. 12373068).

ORCID iDs

Bin Liu https://orcid.org/0000-0002-4875-3429

References

Bandfield, J. L. 2009, Icar, 202, 414
Bandfield, J. L., Hayne, P. O., Williams, J.-P., Greenhagen, B. T., & Paige, D. A. 2015, Icar, 248, 357
Bishop, J. L., Bell, J., & Moersch, J. E. 2019, Remote Compositional Analysis: Techniques for Understanding Spectroscopy, Mineralogy, and Geochemistry of Planetary Surfaces, 24 (Cambridge: Cambridge Univ. Press)
Cambioni, S., Delbo, M., Poggiali, G., et al. 2021, Natur, 598, 49
Cao, H., Zou, M., Zhang, W., et al. 2025, Particuology, 96, 256
Carrier, W. D., III 1973, Moon, 6, 250
Conel, J. E. 1969, JGR, 74, 1614
Conrath, B., Curran, R., Hanel, R., et al. 1973, JGR, 78, 4267
Cooper, B., Salisbury, J., Killen, R., & Potter, A. 2002, JGRE, 107, 5017
Crown, D. A., & Pieters, C. M. 1987, Icar, 72, 492
Davidsson, B. J., Rickman, H., Bandfield, J. L., et al. 2015, Icar, 252, 1
DellaGiustina, D., Emery, J., Golish, D., et al. 2019, NatAs, 3, 341
Donaldson Hanna, K. L., Wyatt, M. B., Thomas, I. R., et al. 2012, JGRE, 117, E00H05
Emery, J., Cruikshank, D., & Van Cleve, J. 2006, Icar, 182, 496
Glotch, T. D., Bandfield, J. L., Lucey, P. G., et al. 2015, NatCo, 6, 6189
Gundlach, B., & Blum, J. 2013, Icar, 223, 479
Hamilton, V., Christensen, P., Kaplan, H., et al. 2021, A&A, 650, A120
Hamilton, V. E. 2010, ChEG, 70, 7
Hanel, R., Conrath, B., Hovis, W., et al. 1972b, Icar, 17, 423
Hanel, R., Schlachman, B., Breihan, E., et al. 1972a, ApOpt, 11, 2625
Hapke, B., Cassidy, W., & Wells, E. 1975, Moon, 13, 339
Heiken, G., McKay, D., & Fruland, R. 1973, in Proc. the Lunar Science Conf., 4, 251
Hunt, G., & Logan, L. 1972, ApOpt, 11, 142
Kieffer, H., Chase, S., Jr., Miner, E., Münch, G., & Neugebauer, G. 1973, JGR, 78, 4291
King, E., Butler, J., & Carman, M. 1972, in Abstracts of the Lunar and Planetary Science Conf., 3, (Lunar and Planetary Science Institute), 449
King, E. A., Butler, J. C., & Carman, M. 1971, in Abstracts of the Lunar and Planetary Science Conf., 2, (Lunar and Planetary Science Institute), 239
King, E. A., Butler, J. C., & Carman, M. F. 1972, in Proc. of the Lunar Science Conf., 3, 673
Lane, M., Mertzman, S., Dyar, M., & Bishop, J. 2011, in 42nd Annual Lunar and Planetary Science Conf., 1608, 1013
Lane, M. D., Glotch, T. D., Dyar, M. D., et al. 2011, JGRE, 116, E08010
Lauretta, D., DellaGiustina, D., Bennett, C., et al. 2019, Natur, 568, 55
Li, J. Q., Xue, L., Zou, M., Zong, W., Xiao, J., et al. 2016, Journal of Jilin University (Engineering and Technology Edition), 46, 172
Logan, L. M., & Hunt, G. R. 1970, JGR, 75, 6539
Logan, L. M., Hunt, G. R., Salisbury, J. W., & Balsamo, S. R. 1973, JGR, 78, 4983
Lucey, P. G., Greenhagen, B. T., Song, E., et al. 2017, Icar, 283, 343
Lyon, R. J. P. 1962, Evaluation of infrared spectrophotometry for compositional analysis of lunar and planetary soils. part ii- rough and powdered surfaces NASA-CR-100[R], Stanford Research Institute
McKay, D. S., Fruland, R. M., & Heiken, G. H. 1974, in Lunar and Planetary Science Conf., 5, 480
McKay, D. S., Heiken, G. H., Taylor, R. M., et al. 1972, in Proc. of the Lunar Science Conf., 3, 983
Morlok, A., Joy, K., Martin, D., Wogelius, R., & Hiesinger, H. 2022, P&SS, 223, 105576
Mustard, J. F., & Hays, J. E. 1997, Icar, 125, 145
Nash, D., & Salisbury, J. 1990, in Abstracts of the Lunar and Planetary Science Conf., 21, 845
Nimura, T., Hiroi, T., & Pieters, C. M. 2008, EP&S, 60, 271
Noble, S. K., Pieters, C. M., Taylor, L. A., et al. 2001, M&PS, 36, 31
Ody, A., Poulet, F., Bibring, J.-P., et al. 2013, JGRE, 118, 234
Okada, T., Fukuhara, T., Tanaka, S., et al. 2020, Natur, 579, 518
Pimentel, G. C., Forney, P. B., & Herr, K. C. 1974, JGR, 79, 1623
Poulet, F., Gomez, C., Bibring, J.-P., et al. 2007, JGRE, 112, E08S02
Presley, M. A., & Christensen, P. R. 1997, JGRE, 102, 6551
Presley, M. A., & Christensen, P. R. 2010, JGRE, 115, E07003
Salisbury, J. W., D'Aria, D. M., & Jarosewich, E. 1991, Icar, 92, 280
Salisbury, J. W., & Eastes, J. W. 1985, Icar, 64, 586
Salisbury, J. W., & Walter, L. S. 1989, JGRB, 94, 9192
Sharkey, B. N., Reddy, V., Malhotra, R., et al. 2021, ComEE, 2, 231
Shirley, K., & Glotch, T. 2019, JGRE, 124, 970
Shirley, K. A. 2018, The Effects of Particle Size and Albedo on Mid-infrared Spectroscopy For The Moon (New York: State University of New York at Stony Brook)
Wang, W., Wang, J., Zhou, K., et al. 2017, IOP Conf. Ser.: Earth Environ. Sci., 81, 012034
Yang, Y., Jiang, T., Liu, Y., et al. 2022, JGRE, 127, e2022JE007453
Yue, W., Biao, W., Xun, W., et al. 2020, Journal of Deep Space Exploration, 7, 371
Zhang, T., Xu, K., & Ding, X. 2021, NatAs, 5, 730